Malignant assignment of neuronal Na^+ leak channel, NALCN: governor of Ca^{2+} oscillations-encoded invadopodogenesis

Oksana Iamshanova[1,13], Dmitri Gordienko[1,13], Antoine Folcher[1], Alexandre Bokhobza[1], George Shapovalov[1], Pascal Mariot[1], Laurent Allart[1], Emilie Desruelles[1], Corentin Spriet[2], Raquel Diez[3], Thibauld Oullier[4], Séverine Marionneau-Lambot[4], Lucie Brisson[5], Sandra Geraci[6], Hathaichanok Impheng[7], V'yacheslav Lehen'kyi[1], Aurelien Haustrate[1], Adriana Mihalache[8], Pierre Gosset[8], Stéphanie Chadet[9], Stéphanie Lerondel[10], Stéphanie Retif[10], Maryline Le Mée[10], Julien Sobilo[10], Sébastien Roger[9], Gaelle Fromont-Hankard[5,11], Mustafa Djamgoz[12], Philippe Clezardin[6], Arnaud Monteil[7], Natalia Prevarskaya[1,14,*]

[1]Univ. Lille, Inserm, U1003 - PHYCEL - Physiologie Cellulaire, F-59000 Lille, France

[2]TISBio, Unité de Glycobiologie Structurale et Fonctionnelle (UGSF), CNRS, UMR 8576, Université de Lille, 59000 Lille, France

[3]Cell Physiology Research Group, Department of Physiology, University of Extremadura, Cáceres, Spain.

[4]Cancéropôle du Grand Ouest, Plateforme In Vivo, 44000 Nantes, France

[5]Inserm UMR1069, Nutrition Croissance et Cancer, University of Tours, 10 boulevard Tonnellé, 37032 Tours, France.

[6]Univ Lyon, Université Claude Bernard Lyon 1, Inserm UMR 1033 LYOS, 69008 Lyon, France.

[7]IGF, CNRS, INSERM, University of Montpellier, LabEx 'Ion Channel Science and Therapeutics', Montpellier, France.

[8]Service d'Anatomie et de Cytologie Pathologiques, Groupement des Hôpitaux de l'Université Catholique de Lille, Lille, France.

[9]EA4245 Transplantation, Immunology, Inflammation, University of Tours, 10 boulevard Tonnellé, 37032 Tours, France

[10]PHENOMIN-TAAM, CNRS UPS44, Centre d'Imagerie du Petit Animal (CIPA), 3B rue de la Férollerie, 45071 Orléans cedex 2, France

[11]CHRU de Tours, Department of Pathology, 2 Boulevard Tonnellé, 37000 Tours, France

[12]Neuroscience Solution to Cancer Research Group, Department of Life Sciences, Faculty of Natural Sciences, Sir Alexander Fleming Building, Imperial College London, South Kensington Campus, London SW7 2AZ, UK.

[13]These authors contributed equally

[14]Lead contact

[*]Correspondence: natacha.prevarskaya@univ-lille.fr

ABSTRACT

Cytosolic Ca^{2+} oscillations provide signaling input to several effector systems of the cell. These include neuronal development, migration and networking. Although similar signaling events are hijacked by highly aggressive cancer cells, the mechanism(s) driving the 'neuron-like' remodeling of the intracellular ionic signature upon cancer progression remains largely elusive. Here, we identify the 'neuronal' Na^+ leak channel, NALCN, in metastatic cells at the hot spots of invadopodia formation and Ca^{2+} event initiation. Mechanistically, NALCN-mediated Na^+ influx associates functionally with plasmalemmal and mitochondrial Na^+/Ca^{2+} exchangers (NCX and NCLX), reactive oxygen species (ROS) and store-operated Ca^{2+} entry (SOCE)/endoplasmic reticulum Ca^{2+} uptake (SERCA) systems to generate intracellular Ca^{2+} oscillations. In turn, the oscillatory activity promotes Src-regulated actin remodeling, Ca^{2+}-dependent secretion of proteolytic enzymes and leads to invadopodogenesis, resulting in tumor progression and metastatic lesions *in vivo*. Thus, we have uncovered malignant assignment of NALCN giving rise to a critical intracellular Na^+/Ca^{2+} signaling axis.

Sodium leak channel, calcium oscillations, Src kinase, vesicle secretion, invasion, metastasis, oncochannelopathy.

INTRODUCTION

Over the years, several studies have revealed some striking similarities in the behavior between neuronal and metastatic cancer cells (Onganer et al., 2005; Santiago-Medina et al., 2015; Short et al., 2016). Indeed, gene products traditionally known for their role in normal neuronal migration, axonal growth and embryonic development, were also pinpointed in metastasis, where they contribute to the aggressive cancer phenotype (Biankin et al., 2012; Monk and Holding, 2001; Shah et al., 2018). Interestingly, ion channels responsible for cell excitability were also reported for metastatic cells. For example, voltage-gated Na^+ channels (VGSCs), also involved in neurite outgrowth, were shown to be expressed *de novo* in several human carcinomas where they serve to conduct Na^+ current and promote cancer cell invasiveness (Djamgoz et al., 2019; Patel and Brackenbury, 2015; Roger et al., 2015). Another neuronal protein, the redox-sensing channel transient receptor potential ankyrin 1 (TRPA1), was also described to be overexpressed in diverse tumor types, where it mediates oxidative stress tolerance in cancer cells via activation of Ca^{2+}-dependent anti-apoptotic pathways by TRPA1-mediated Ca^{2+} influx (Takahashi et al., 2018).

One of the major features of the living cell, transmembrane ion gradients, is paid for by substantial cellular resources serving ion transportation (Clapham, 2007; Verkhratsky et al., 2018). Being involved in signal transduction, these ion gradients are temporally and spatially encoded. Particularly, time-dependent changes in cytosolic Ca^{2+} concentration ($[Ca^{2+}]_c$) may appear as oscillations comprising repetitive spikes and/or Ca^{2+} waves (Dupont et al., 2011). Specific spatiotemporal encoding of these signals allows

transmission of key intracellular messages avoiding damages associated with sustained $[Ca^{2+}]_c$ elevations (Smedler and Uhlén, 2014). Accordingly, $[Ca^{2+}]_c$ oscillations have been implicated in numerous physiological cellular processes including gene expression, fertilization, cellular motility, muscle contraction, secretion and synaptic transmission (Berridge, 2008; Dolmetsch et al., 1998; Pasti et al., 1997; Savineau and Marthan, 2000; Wakai et al., 2011). The role of Ca^{2+} signaling in carcinogenesis is also now well acknowledged (Iamshanova et al., 2017; Monteith et al., 2017; Prevarskaya et al., 2018) with $[Ca^{2+}]_c$ oscillations suggested as a hallmark of cancer cell aggressiveness leading to metastases dissemination (Catacuzzeno and Franciolini, 2018; Rizaner et al., 2016; Sun et al., 2014; Tang et al., 2015). Therefore, understanding the mechanisms of alterations in ionic homeostasis that drives metastatic phenotype is necessary to improve both the survival and the everyday life of cancer patients.

Ca^{2+} oscillations may be driven by various pacemaker inputs. Among them, a good candidate is the Na^+ leak channel, NALCN, that was shown to regulate neuronal excitability, synaptic transmission fidelity and rhythmic activity via modulation of membrane ion permeability (Jospin et al., 2007; Lu et al., 2007; Yeh et al., 2008). Moreover, NALCN was suggested to regulate neuronal axonal growth via the Rho guanine nucleotide exchange factor, Trio (Topalidou et al., 2017). Since Trio was shown to be implicated in controlled turnover of invadopodia during cancer cell invasion, it raised the possibility of NALCN involvement in tumorigenesis (Kwiatkowska et al., 2012; Moshfegh et al., 2014). Furthermore, the elevated tissue Na^+ concentration has been found to be a highly specific *in vivo* indicator of malignancy, which can be, at least in part, provided by sustained NALCN-mediated Na^+ influx (Barrett et al., 2018; Bartha et al., 2008; Haneder et al., 2015; Henzler et al., 2012; Huang et al., 2018; Jacobs et al., 2011; Laymon et al., 2012; Leslie et al., 2019; Ouwerkerk et al., 2003, 2007; Zaric et al., 2016). Given the tight coupling between Na^+ and Ca^{2+} signaling (Verkhratsky et al., 2018), we hypothesized that in metastatic cancer cells NALCN could provide signaling input encouraging the cell invasion via intracellular Ca^{2+} events.

Our findings identify the neuronal Na^+ leak channel, NALCN, as a major mechanism responsible for Na^+ influx that governs Ca^{2+} oscillations (respectively in the cytoplasm, endoplasmic reticulum and mitochondria), ROS production and initiation of invadopodia formation (referred hereafter as invadopodogenesis) in strongly metastatic prostate cancer cells. Importantly, formation of dynamin puncta, reporting invadopodial precursor assembly, occurred at sites of the $[Ca^{2+}]_c$ wave initiation enriched with NALCN. The NALCN-governed oscillatory Ca^{2+} events facilitate secretion of proteolytic enzymes (matrix metalloproteinases, MMPs) and promote invadopodogenesis via Src kinase activation and actin remodeling (also encouraged by N-WASP – Cdc42 coupling). Modulation of NALCN bioavailability strongly affects *in vivo* prostate cancer progression and bone metastasis formation.

Overall, our study uncovers malignant assignment of NALCN and demonstrates its role as the central element of critical Na^+/Ca^{2+} signaling axis promoting metastatic progression.

RESULTS AND DISCUSSION

NALCN Promotes Metastasis-Associated Cancer Cell Behavior

Initial immunohistochemical analysis of human prostate tissue arrays detected NALCN upregulation during cancer progression (Figure S1A). Consistent with this, screening of various prostate cancer cell lines revealed NALCN and all members of the NALCN channelosome - UNC-79, UNC-80 and NLF-1 (Cochet-Bissuel et al., 2014) - only in highly aggressive cell lines, with little or no expression in weakly metastatic cells (Figures S1B and S1C). Furthermore, NALCN was functionally expressed in the plasma membrane (PM) (Figure S1D), thus providing a pathway for Na^+ influx, which was not observed in NALCN-negative cell lines (Figures S1E-S1G). Importantly, NALCN silencing did not affect cellular viability, cell cycle progression, apoptosis (basal or induced) or proliferation, whereas metastasis-associated behaviors (cellular motility, migration and invasion) were significantly dependent on the level of NALCN expression (Figure S2, S7A-C, S7G). Recruitment of NALCN to invadopodogenesis was confirmed by cyanine-3 (Cy3)-fluorescent gelatinase assay. Thus, NALCN silencing significantly suppressed the number of the invadopodium formation sites and the total area of gelatin degradation (Figures 1A and S2F). It was previously shown that Na^+ influx via voltage-gated Na^+ channels (VGSCs) facilitates H^+ extrusion by an allosteric modulation of the Na^+/H^+ exchanger type 1 (NHE-1) at focal ECM degradation sites, thus leading to acidification of the pericellular microenvironment and activation of cysteine cathepsins that promotes metastasis (Brisson et al., 2011, 2013; Gillet et al., 2009). Surprisingly, NALCN depletion had no effect on intracellular pH nor H^+ extrusion from the cells (Figure S2G). This raised the possibility that a mechanism other than pH couples the NALCN-mediated Na^+ influx to promotion of metastasis. When PC-3 cells co-expressing NALCN-GFP and RCamp (to label the cell body) were placed on gelatin, newly formed invadopodia appeared enriched with NALCN (Figure 1B). NALCN expression in invadopodia was confirmed further by subcellular fractionation (Figure S2P). Finally, immunocytochemical analysis revealed strong co-localization of NALCN with Src kinase (a key signaling component of invadopodogenesis) and other invadopodial proteins (cortactin, dynamin, matrix metalloproteinase MT1-MMP and adaptor protein Tks5) within specific morphological structures referred to as 'invadopodia puncta and rosettes' (Figures 1C and S2Q). Although previous studies reported that Src kinase is recruited to the NALCN channelosome, no evidence of direct Src kinase dependence on NALCN expression was presented (Lu et al., 2009; Wang and Ren, 2009). We found that NALCN knockdown (NALCN-KD) markedly suppressed both Src kinase expression and activity in metastatic PC-3 cells (Figure S2N and S2O).

Invadopodia share molecular, structural and functional characteristics with analogous neuronal structures (filipodia and lamelipodia) responsible for axonal growth, branching and networking (Santiago-Medina et al., 2015). At the same time, synaptic transmission and neuronal excitability were recently demonstrated to rely on the modulation of plasma membrane conductance by NALCN (Yeh et al., 2008). Specifically, a

high degree of correlation between the genesis of the synaptic Ca^{2+} transients and NALCN activity was reported (Yeh et al., 2008).

It was previously demonstrated that stimulation of starved melanoma cells with fetal bovine serum (FBS) induces Ca^{2+} oscillations and facilitates invasion (Sun et al., 2014). However, the casual link between the two processes remained unknown. We found in PC-3 cells also that FBS-induced $[Ca^{2+}]_c$ response, associated with deviation of $PI(4,5)P_2$ (phosphatidylinositol 4,5-bisphosphate) from equilibrium, facilitated interaction between N-WASP (neuronal Wiskott–Aldrich syndrome protein) and Cdc42 (cell division cycle 42 protein), and induced invadopodial precursor assembly detectable as enriched F-actin and dynamin puncta (Figure S3). Importantly, this process was strongly suppressed by NALCN-KD (Figure 1D). Notably, the FBS-induced formation of dynamin puncta, reporting invadopodial precursor assembly, occurred at sites of the $[Ca^{2+}]_c$ wave initiation (Figure 1E). The latter coincided with NALCN-enriched rosette forming cap-like structure at the cell bottom (Figures 1F and 1G).

NALCN Regulates Vesicular Secretion of ECM-Degrading Enzymes in Ca^{2+}-Dependent Manner

In cancer cells, vesicular secretion of ECM-degrading enzymes is the principal mechanism facilitating extracellular proteolysis and invasion. However, whether this secretion is a Ca^{2+}-dependent process, is not known. We found that vesicle secretion in PC-3 cells is controlled by $[Ca^{2+}]_c$ in microdomains, since both fast and slow Ca^{2+} chelators suppressed this process to different extents (Figures 2A and 2E). Importantly, the presence of NALCN proved a critical determinant of the rate of vesicle secretion by PC-3 cells (Figures 2B and 2C). Consistent with this NALCN also controlled the activity of ECM-degrading enzymes (Figure 2D).

Taken together, these results strongly suggested that the signaling underlying the input of NALCN to invadopodogenesis and cancer cell invasiveness should involve $[Ca^{2+}]_c$ events.

NALCN Drives Ca^{2+} Oscillations

We found that FBS or epidermal growth factor (EGF) alone induced an initial $[Ca^{2+}]_c$ transient followed by $[Ca^{2+}]_c$ oscillations with reciprocal changes of Ca^{2+} concentration in the endoplasmic reticulum ($[Ca^{2+}]_{ER}$) (Figures 3A and 3B). The initial $[Ca^{2+}]_c$ transient, but not the subsequent $[Ca^{2+}]_c$ oscillations, persisted in Ca^{2+}-free solution supplemented with 0.5 mM EGTA, while both were abolished following Ca^{2+} store depletion with 50 µM cyclopiazonic acid (CPA) even when the cells were bathed in Ca^{2+}-containing solution (Figure 3C). We concluded, therefore, that these $[Ca^{2+}]_c$ oscillations depend on both repetitive Ca^{2+} influx and Ca^{2+} recycling by the ER. To assess the role of NALCN in the $[Ca^{2+}]_c$ oscillations, we compared spatiotemporal patterns of the FBS-induced $[Ca^{2+}]_c$ response in serum-starved PC-3 cells in control and following NALCN silencing (Figures 3D and 3E). This revealed that the FBS-induced $[Ca^{2+}]_c$ oscillations (both frequency and signal mass temporal density) were attenuated significantly in NALCN-KD cells (Figure 3F). Also, the Ca^{2+} "pacemaker phase" observed in these

oscillations was also under the control of NALCN (Figures 3D and 3E). The $[Ca^{2+}]_c$ oscillations were attenuated dramatically by reduction of extracellular Na^+ concentration ($[Na^+]_o$) (Figure 3G). Furthermore, the FBS-induced inward current was suppressed by NALCN-KD or $[Na^+]_o$ reduction (Figure 3H). These findings were substantiated by a reversed strategy: NALCN overexpression significantly increased FBS-induced inward current and the $[Ca^{2+}]_c$ oscillations (Figure S7C-F).

These results demonstrated directly that the FBS-induced $[Ca^{2+}]_c$ oscillations are governed by NALCN-mediated Na^+ influx. In addition, stimulation with FBS (which triggered $[Ca^{2+}]_c$ oscillations) increased Src kinase activity in serum-starved PC-3 cells (Figure S4A).

In conclusion, in these strongly metastatic prostate cancer cells, NALCN enhances Src kinase activity by promoting $[Ca^{2+}]_c$ oscillations, which depend on (i) NALCN-mediated Na^+ influx (Figures 3D-3H) and (ii) repetitive Ca^{2+} influx and Ca^{2+} recycling by the ER (Figures 3A-3C).

A number of Na^+-permeable channels were suggested to influence $[Ca^{2+}]_c$ events in different cell models (Verkhratsky et al., 2018). In cancer cells, functional coupling of VGSC activity to intracellular Ca^{2+} signaling was predicted in human colon cancer (House et al., 2010). Later, it was shown that spontaneous $[Ca^{2+}]_c$ oscillations in strongly metastatic human prostate and breast cancer cells were inhibited by VGSCs blockers (Rizaner et al., 2016). However, the molecular mechanisms coupling Na^+ influx to $[Ca^{2+}]_c$ oscillations as well as their role in metastatic cell behavior remained unknown.

Coupling Between NALCN-Mediated Na^+ Influx and $[Ca^{2+}]_c$ Events

Oscillations generally require positive feed-back between the contributing elements. We, therefore, assessed (i) modulation of NALCN-mediated Na^+ influx by extracellular Ca^{2+} concentration ($[Ca^{2+}]_o$) as well as by the events leading to $[Ca^{2+}]_c$ elevation and (ii) coupling between Na^+ influx and rise of $[Ca^{2+}]_c$. To unravel the net effect of $[Ca^{2+}]_c$ elevation on NALCN-mediated Na^+ influx, we assessed the Na^+ influx induced by switching $[Na^+]_o$ from 0 to 130 mM (Figure 4A) and by store-operated Ca^{2+} entry (SOCE) (Figure 4C). The two were then compared (Figure 4D, top). We found that the $[Na^+]_o$ switch induced a significant Na^+ influx (Figure 4A) that: (i) was dramatically suppressed by NALCN-KD (see also Figure 4D); (ii) was not modulated by $[Ca^{2+}]_o$, at least within the range of 0 – 4 mM (see also Figure S4B), in contrast to that previously reported for neurons (Lu and Feng, 2012; Lu et al., 2010); and (iii) was not affected by Ca^{2+} store depletion (see also Figure S4C). Furthermore, $[Ca^{2+}]_c$ elevation brought about by acute inhibition of sarco/endoplasmic reticulum Ca^{2+}-ATPase (SERCA) with thapsigargin (TG) failed to induce Na^+ influx when the cells were bathed in Ca^{2+}-free external solution supplemented with 0.5 mM EGTA, *i.e.* when SOCE was prevented (Figure 4B). Moreover, we have found (Figure 4C) that: (i) SOCE activation triggers Na^+ influx even at constant physiological $[Na^+]_o$ in a $[Ca^{2+}]_o$-dependent manner (see also Figures S4D-S4G); (ii) NALCN-KD significantly suppresses not only this Na^+ influx but also SOCE; and (iii) inhibition of the reverse-mode plasmalemmal Na^+/Ca^{2+} exchanger (RM-NCX) curtails $[Ca^{2+}]_c$

transient caused by SOCE at $[Na^+]_o$=130 mM, does not affect it at $[Na^+]_o$=0 mM and attenuates $[Ca^{2+}]_c$ transient triggered by Na^+ readmission following SOCE activation. Comparison of the effects of NALCN-KD on Na^+ influx caused by the $[Na^+]_o$ switch with that triggered by SOCE revealed that SOCE significantly augmented NALCN-mediated Na^+ influx (Figure 4D, top). In addition, the cell-surface biotinylation assay reported that SOCE increased expression of NALCN protein in PM (Figure 4D, bottom), similar to FBS (Figure S4H).

The above results indicate that Ca^{2+} influx during SOCE (Figures 4C and 4D), but not Ca^{2+} release from the ER (Figure 4B) or Ca^{2+} store depletion *per se* (Figure 4A, right), enhances NALCN-mediated Na^+ influx by addressing NALCN protein to the PM. In turn, the rise in cytosolic Na^+ concentration ($[Na^+]_c$) facilitates Ca^{2+} influx either via RM-NCX (Figures 4C, middle, and S4I) and/or by relieving SOCE inactivation. The latter may involve mitochondrial Na^+/Ca^{2+} exchanger (NCLX), which was shown previously to be capable of modulating reactive oxygen species (ROS) production and, hence, SOCE (Ben-Kasus Nissim et al., 2017). We found that NCLX silencing indeed suppressed SOCE (Figures 4C, right, and S4J). This suggests the following signaling cascade in PC-3 cells: NALCN-mediated Na^+ influx → NCLX-mediated Ca^{2+} extrusion from mitochondria → decrease of ROS production → relief of SOCE inactivation. At the same time, attenuation of the FBS-induced $[Ca^{2+}]_c$ events (both the initial transient and oscillations) by the RM-NCX inhibitor KB-R7943 (Figure 4E), suggests that NALCN-mediated Na^+ influx facilitates RM-NCX-mediated Ca^{2+} entry, while inhibition of FBS-induced inward current by this compound (Figure 4F) indicates that this Ca^{2+} entry encourages NALCN-mediated Na^+ influx. It is this positive feed-back between NALCN and RM-NCX that is likely to sustain the $[Ca^{2+}]_c$ oscillations. The modulation of the feedback via the ER Ca^{2+} recycling is also tuned by SOCE and RM-NCX (Figure 3A). We also verified that the Na^+ influx, attributed to the NALCN-mediated current in PC-3 cells, is tetrodotoxin-resistant and gadolinium-sensitive, similar to neuronal NALCN (Figures S4K-S4P) (Lu et al., 2007).

NALCN – NCLX Functional Coupling Recruits Mitochondria to Regulation of $[Ca^{2+}]_c$ Oscillations

The tight functional coupling between SOCE and NALCN (Figures 4C and 4D), the dependence of $[Ca^{2+}]_c$ oscillations on NALCN-mediated Na^+ influx (Figures 3D-3G) and the involvement of NCLX in SOCE regulation (Figure 4C, right) via ROS-mediated oxidation of Ca^{2+} release-activated Ca^{2+} channel protein 1 (Orai1) (Ben-Kasus Nissim et al., 2017) suggest that, apart from RM-NCX, the NALCN-mediated Na^+ influx may also regulate $[Ca^{2+}]_c$ oscillations via NCLX. Indeed, the latter would exchange mitochondrial Ca^{2+} to Na^+ delivered via NALCN, and hence oppose Ca^{2+} uptake by the mitochondrial Ca^{2+} uniporter (MCU) and subsequent ROS production. Consistent with this, we observed that the FBS-induced $[Ca^{2+}]_c$ oscillations were associated with oscillations of (i) Ca^{2+} concentration in mitochondria ($[Ca^{2+}]_{mito}$; Figure 5A) and (ii) mitochondrial superoxide ($O_2^{\dot{\circ}-}$) production (Figure 5B). Also, application of H_2O_2 (endogenous product of $O_2^{\dot{\circ}-}$) suppressed the $[Ca^{2+}]_c$ oscillations (Figure 5C). In support of the

above hypothesis, we have also found that NCLX silencing (siNCLX) dramatically attenuated the FBS-induced $[Ca^{2+}]_c$ oscillations (Figure 5D). Interestingly, the initial $[Ca^{2+}]_c$ transient caused by the FBS application had significantly longer duration in cells pre-treated with siNCLX, likely to be due to suppression of SERCA by enhanced ROS production in mitochondria lacking NCLX (Qin et al., 2014). Thus, interplay between Ca^{2+} and Na^+ signals not only would affect mitochondrial Ca^{2+} shuttling and mitochondrial redox status (Ben-Kasus Nissim et al., 2017), but also serve to maintain persistent $[Ca^{2+}]_c$ oscillations. In turn, the latter are necessary for Src activation (Sun et al., 2014) and the Ca^{2+}-dependent vesicular secretion of ECM-degrading enzymes (Figure 2).

NALCN Promotes Prostate Cancer Aggressiveness *In Vivo*

We found that *NALCN* mRNA level was significantly higher in prostate cancer biopsies relative to non-cancerous tissues taken from the same patients (Figure 6B). In addition, immunohistochemical analyses revealed that NALCN was not detected in non-cancerous prostate glands (Figure 6A). In human prostate cancer, NALCN immunostaining was observed in 57% of clinically localized hormone-naïve cases, 6% (3/48) of castration-resistant prostate cancer (CRPC) and 62% (13/21) of metastases. In clinically localized prostate cancer, NALCN expression was significantly higher within the ISUP group (Gleason score that reflects loss of differentiation) (Table S1). NALCN expression was also significantly higher in pT3 tumors (with extra-prostatic extension) than in pT2 tumors (limited to the prostate gland) (Table S1). In clinically localized prostate cancer, the expression of NALCN was strongly correlated with the expression of Src-kinase (Figure 6A). Similar results were obtained for NALCN expression in other cancers: positive staining in bone metastases from breast (11/19) and colon (5/8) cancers, without any detectable expression in corresponding normal tissues (0/5) (Figure 6C). These data suggested (i) that the *in vitro* results described above have clinical relevance and (ii) that NALCN may play similar malignant role in several carcinomas.

Finally, we analyzed the role of NALCN in cancer progression *in vivo* by using several mice models.

Since phosphatase and tensin homologue (PTEN) is one of the most commonly deleted/mutated tumor suppressor genes in human prostate cancer, we utilized the PTEN knockout mouse with conditional gene inactivation (floxed allele; L2) as our first *in vivo* model (Parisotto et al., 2018). Following prolonged treatment with tamoxifen, $PTEN^{-/-}$ mice produced prostate adenocarcinoma, whereas $PTEN^{-/-}p53^{-/-}$ developed more aggressive and invasive phenotype of prostate cancer. *Ex vivo* analysis performed on these prostate tumors revealed that NALCN was markedly upregulated in $PTEN^{-/-}p53^{-/-}$ tumors (i.e. during progression of invasive adenocarcinoma), compared with the $PTEN^{-/-}$ tumors (i.e. during initial tumorigenesis) (Figure 6D).

To study the progression of prostate tumors *in vivo*, we developed xenografts of PC-3 cells with stable luciferase activity. Therefore, our second *in vivo* model was presented by the nude mice that were injected

orthotopically with these cells and followed for 12 weeks, allowing primary tumor growth and metastases development. We found that NALCN-KD significantly suppressed metastasis and primary tumor growth *in vivo* (Figures S5A-S5C). This was confirmed further by *ex vivo* analyzes (Figures S5D and S5E). It is well known that prostate cancer frequently metastasizes to bone (in fact, the PC-3 cell line was originally derived from the bone metastases of a prostate cancer patient). We observed that injection of NALCN-KD PC-3 cells caused significantly less skeletal metastases than that of control (Figure 6E). NALCN-KD also induced a reduction of metastasis to other organs, albeit to a lesser extent (Figures S5D and S5E).

The above observations supported our hypothesis that NALCN expression determines metastatic potential of PC-3 cells, specifically to the bone. Indeed, Transwell® invasion assay utilizing osteoblast conditioned media as a chemoattractant showed significant decrease of the invasiveness in PC-3 cells with NALCN-KD (Figure 6F). Furthermore, the direct injection of PC-3 cells into tibia of nude mice (third *in vivo* model) revealed that the cells with NALCN-KD produced significantly reduced bone tissue destruction, compared with control cells (Figures 6G and Figure S6). In contrast, assessment of the effect of intracardiac injection (fourth *in vivo* model) of permanently NALCN-overexpressing PC-3 cells revealed that, in control group (PC-3 Luc) 18% of mice (2/11) developed one unique osteolytic lesion (both were located in the fibula), while in cells stably overexpressing NALCN (+hNALCN) 64% of mice (7/11) developed multiple osteolytic lesions of larger volumes (Figurex S7H and S7I) in different bone locations (fibula, tibia, hip, humeral, skull and jaw bones).

Results from all four *in vivo* mice models were consistent, indicating that the level of NALCN expression directly correlated with the metastatic impact of PC-3 derived tumor xenografts.

CONCLUSIONS

In this study, we identified for the first time that the expression of NALCN is upregulated in human prostate carcinoma samples compared to normal tissues in which it is not detected. We have found that NALCN is functional and importantly promotes invasiveness and metastatic potential of prostate cancer cells by controlling the Na^+/Ca^{2+} signature. Specifically, we demonstrated a novel NALCN-mediated mechanism of cancer cell aggressiveness whereby long-term intracellular Ca^{2+} oscillations are the central player. These oscillations are controlled mainly by SOCE, NCX, NCLX, SERCA and ROS, and are necessary for Src kinase activation, invadopodia formation and Ca^{2+}-dependent vesicular secretion of ECM degrading enzymes (Figure 7). Furthermore, results from several mice models suggested that NALCN expression promoted the metastatic impact of prostate cancer *in vivo*.

In overall conclusion, our study identifies a novel ionic checkpoint during the metastatic transformation and pinpoint NALCN as a key player governing this process in prostate cancer.

MAIN FIGURES WITH LEGENDS

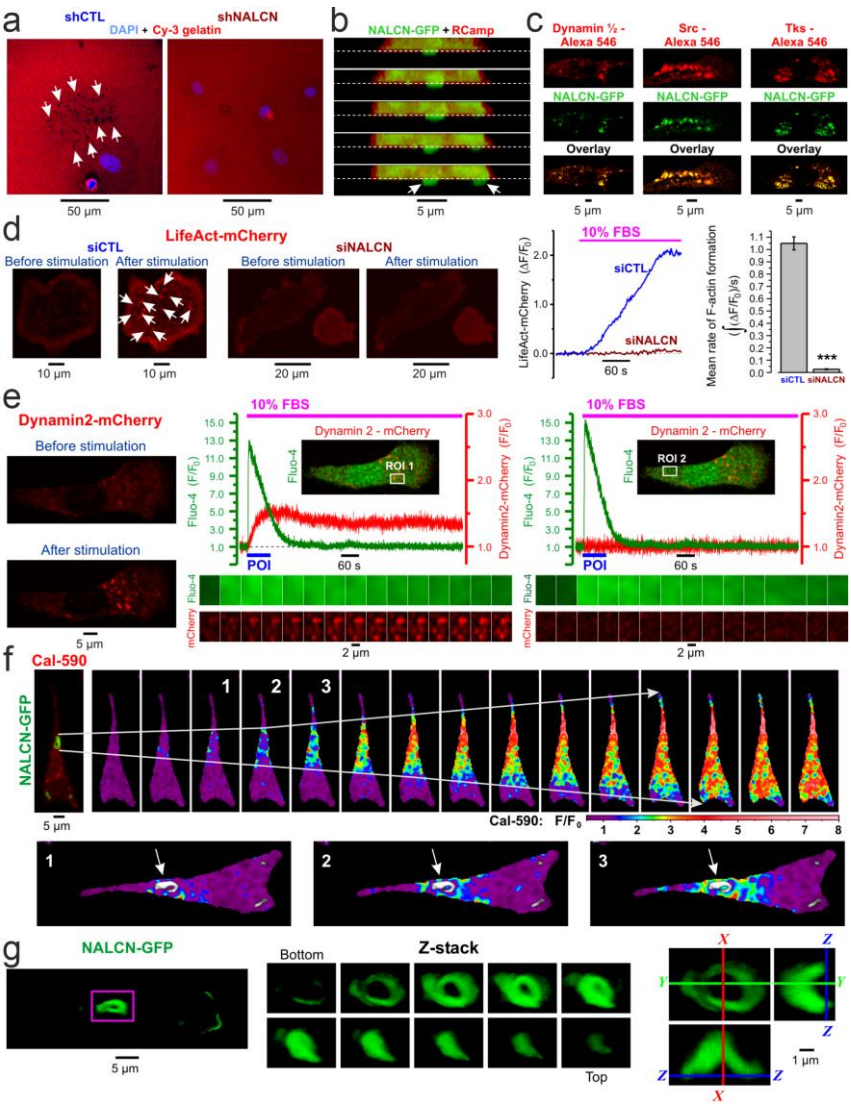

Figure 1. NALCN Provides Signaling Input to Invadopodia in PC-3 Cells.
(**a**) NALCN knockdown suppresses invadopodium formation revealed by Cy3-fluorescent gelatin degradation (arrows). Confocal images of Cy3 (red) and DAPI (blue; nuclei) fluorescence in control (shCTL) and NALCN depleted cells (shNALCN) 48 hours after plating the cells on gelatin. (**b**) Sequential (top to bottom) *z-x* confocal cross-sections of the cell transfected with green fluorescent protein (GFP)-tagged NALCN and red Ca^{2+} binding protein (RCamp) reveal localisation of NALCN in newly-formed invadopodia (arrows). Dashed lines: gelatin surface. (**c**) Co-localisation of NALCN with invadopodia markers: Dynamin (left), Src (middle) and Tks (right).
(**d**) NALCN silencing suppresses invadopodial precursor assembly (arrows: F-actin-enriched regions reported by LifeAct-mCherry). Left: near-cell-bottom confocal images captured before and 3 min after stimulation with 10% fetal bovine serum (FBS). Middle: corresponding traces of relative changes in mCherry fluorescence. Right: mean rate of F-actin formation estimated as signal mass ($\int(\Delta F / F_0)$) per second in cells transfected for 72 hours with siRNA targeting firefly luciferase (siCTL, n=93) and with siRNA-1 (siNALCN, n=140) and compared. Data are mean±S.E.M. ***P<0.001, two-tailed Student's t-test. (**e**) Left: confocal images of Dynamin2-mCherry fluorescence captured before and 3 min after stimulation with 10% FBS. Middle and right: plots relates the dynamics of cytosolic Ca^{2+} ($[Ca^{2+}]_c$) changes (Fluo-4) to formation of dynamin puncta (Dynamin2-mCherry) at two regions of interests (ROIs) (insets); the galleries (below) show (left to right) every 40th image (after 90° rotation) during the points of interest (POIs) (plots: blue bars). (**f**) Top: the overlay of NALCN-GFP and Cal-590 images (left) is related to the gallery of self-normalized rainbow-coded Cal-590 images showing $[Ca^{2+}]_c$ response to 10% FBS. Bottom: 3 rainbow-coded Cal-590 images are superimposed on grey-coded NALCN-GFP image. Arrows: NALCN-enriched structure. (**g**) 3-D distribution of NALCN in the region of Ca^{2+} wave initiation: confocal *z*-sections (middle) of the boxed region (left) and corresponding *x-y*, *z-y* and *z-x* cross-sections (right). See also Figures S1-S3.

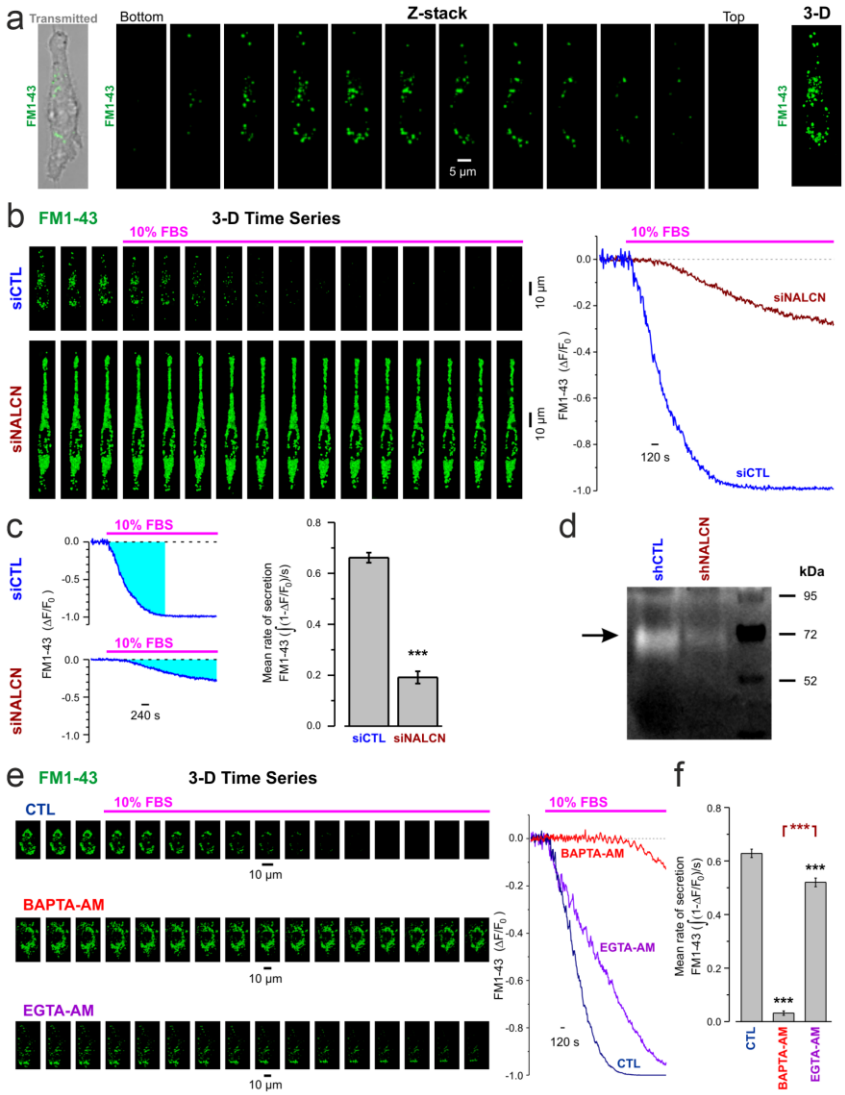

Figure 2. NALCN Regulates Vesicular Secretion of ECM-Degrading Enzymes in Ca^{2+}-Dependent Manner. (**a**) 3-D distribution of FM1-43-labelled secretory vesicles in PC-3 cell. Left: overlay of transmitted and *x-y* confocal images of FM1-43 fluorescence. Middle: confocal *z*-sections. Right: corresponding 3-D image. (**b**) Left: the galleries of sequential 3-D images (every 25th image) compare FBS-induced degradation of FM1-43-labelled secretory vesicles in PC-3 cells pre-treated with siCTL and siNALCN. Right: corresponding traces of relative changes in total z-stack fluorescence. (**c**) Plot compares mean rates of secretion, calculated as signal mass (cyan, left) per second, in control (siCTL: n=35) and following NALCN suppression (siNALCN: n=40). (**d**) Zymography compares gelatinase activity (72 kDa) in shCTL and shNALCN. (**e**) The same as (**b**) but for untreated (CTL) cells and those loaded with slow (EGTA-AM: n=35) and fast (BAPTA-AM) Ca^{2+} chelators. (**f**) The same as (**c**) but compares the mean rates of secretion in CTL (n=45) and after treatment with EGTA-AM (n=35) or BAPTA-AM (n=62). Data are mean±S.E.M. ***P<0.001, two-tailed Student's *t*-test.

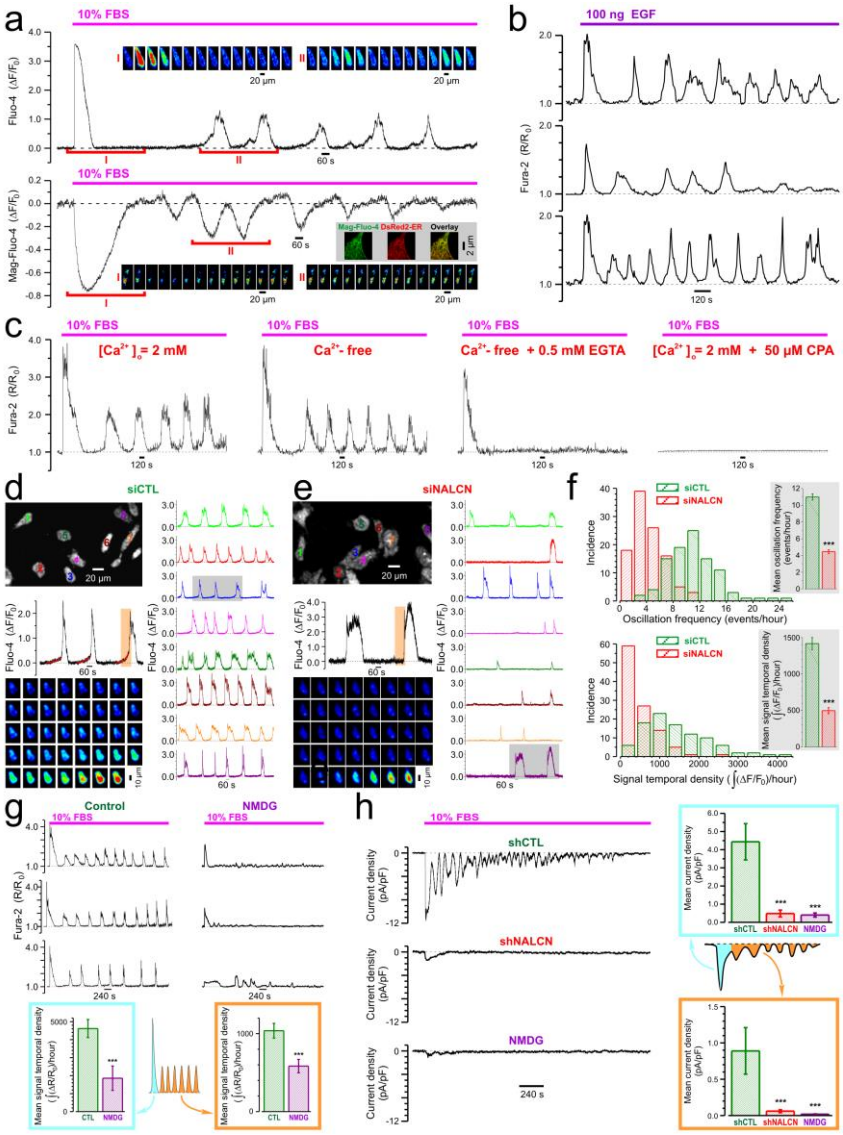

Figure 3. NALCN Regulates Ca^{2+} Oscillations in PC-3 Cells.
(**a**) Fetal bovine serum (FBS)-induced transient cytosolic Ca^{2+} ($[Ca^{2+}]_c$) elevations (Fluo-4, top) are associated with transient decreases of Ca^{2+} concentration in endoplasmic reticulum ($[Ca^{2+}]_{ER}$) (Mag-Fluo-4, bottom). The galleries (insets) show every 100th image during the highlighted periods (I and II, respectively). Visualisation of the ER with pDsRed2-ER vector confirms the ER origin of Mag-Fluo-4 signal (grey background inset: confocal images of cell fragment). (**b**) Sample traces of epithelial growth factor (EGF)-induced $[Ca^{2+}]_c$ responses (Fura-2). (**c**) Contribution of Ca^{2+} influx and Ca^{2+} release to FBS-induced $[Ca^{2+}]_c$ response (Fura-2) illustrated by sample traces (left to right): control, nominally Ca^{2+}-free or EGTA-supplemented solutions, and Ca^{2+}-containing solution but depleted Ca^{2+} stores. (**d** and **e**) $[Ca^{2+}]_c$ oscillations reported by confocal time-series imaging of Fluo-4 fluorescence in FBS-exposed PC-3 cells pre-treated with siCTL (D) or siNALCN (E) for 72 hours. The trace colours (right) correspond to the colour of the cell number (top left). Highlighted (grey background) periods are presented on enlarged plots (left middle) to emphasise that NALCN suppression abolishes "pacemaker events" observed in control (fitted red curves). The galleries (left bottom) show every 3rd image during the highlighted periods (left middle: orange background). (**f**) The histograms compare the oscillation frequency (top) and signal temporal density (bottom) distributions for siCTL (n=98) and siNALCN (n=107). Insets: corresponding mean±S.E.M. ***P<0.001, two-tailed Student's t-test. (**g**) FBS-induced $[Ca^{2+}]_c$ response (Fura-2, $\Delta R/R_0$) is attenuated following reduction of extracellular Na^+ concentration ($[Na^+]_o$) to 19.5 mM (substitution with NMDG). (**h**) FBS-induced inward current (perforated patch, V_h=-80 mV) is suppressed following pre-treatment with shNALCN or reduction of $[Na^+]_o$ to 13 mM (substitution with NMDG). The bar diagram plots: mean signal temporal densities (**g**, n=20-23) and mean current densities (**h**, n=4-6) during initial transient (cyan) and oscillations (orange). Data are mean±S.E.M. ***P<0.001, two-tailed Mann-Whitney U test.

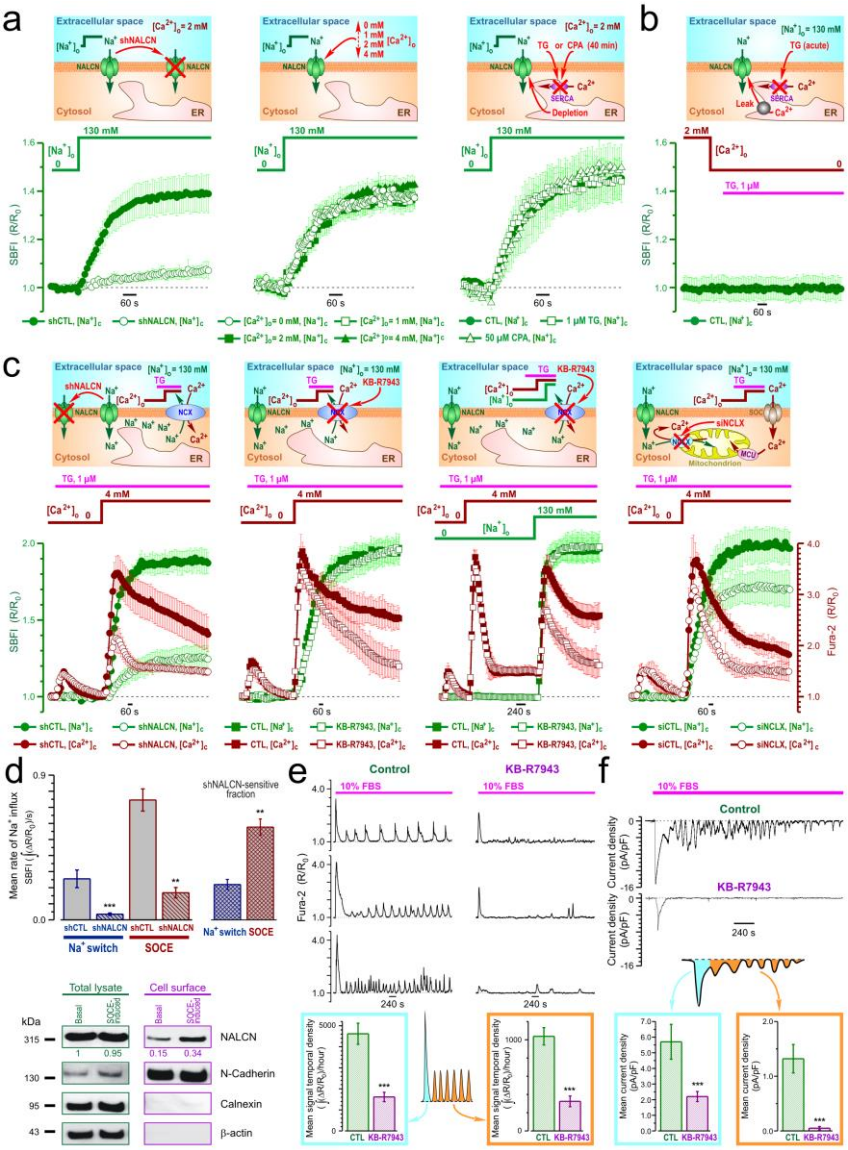

Figure 4. Interplay between SOCE, NALCN, NCX and NCLX in PC-3 Cells.
(**a** and **b**) Extracellular Na^+ concentration ($[Na^+]_o$) changes reported by ratiometric Na^+ indicator SBFI following (**a**) $[Na^+]_o$ switch from 0 to 130 mM and (**b**) application of 1 μM thapsigargin (TG), the sarco/endoplasmic reticulum (SERCA) inhibitor uncoupling the endoplasmic reticulum (ER) Ca^{2+} leak from Ca^{2+} re-uptake into the ER. In (**a**) the effect of (left to right): NALCN knockdown, extracellular Ca^{2+} concentration ($[Ca^{2+}]_o$) and Ca^{2+} store depletion. (**c**) Store-operated Ca^{2+} entry (SOCE)-induced changes of cytosolic Na^+ concentration ($[Na^+]_c$) (SBFI) and cytosolic Ca^{2+} concentration ($[Ca^{2+}]_c$) (Fura-2); the effect of (left to right): NALCN knockdown, the reverse-mode plasmalemmal Na^+/Ca^{2+} exchanger (RM-NCX) inhibitor KB-R7943 (1 μM) at $[Na^+]_o$=130 mM and $[Na^+]_o$ stepped from 0 to 130 mM following SOCE activation, and knockdown of the mitochondrial Na^+/Ca^{2+} exchanger (siNCLX). In (**a-c**) cartoons (top) highlight experimental design and plots (bottom) show traces (mean±S.E.M; *n*=45-501) of SBFI (olive) and Fura-2 (wine) fluorescence with the axes (R/R_0) presented in corresponding colour. (**d**) SOCE addresses NALCN to plasma membrane. Plots (top) compare mean rates of Na^+ influx induced by $[Na^+]_o$-switch (*n*=283-360) and SOCE (*n*=180-216), and their shNALCN-sensitive fractions. Immunoblotting (bottom) compares NALCN expression in total cell lysates and biotinylated fractions before and following SOCE induction. Numbers show (in corresponding colour) mean values (*n*=3) of NALCN protein levels (band intensity) normalized to N-Cadherin, Calnexin and β-actin. (**e** and **f**) KB-R7943 (1 μM) attenuates: (**e**) $[Ca^{2+}]_c$ responses (Fura-2, R/R_0) and (**f**) inward current (perforated patch, V_h=-80 mV) induced by 10% FBS. The bar diagram plots: mean signal temporal densities (**e**, *n*=20) and mean current densities (**f**, *n*=6-8) during initial transient (cyan) and oscillations (orange). Data are mean±S.E.M. ***P*<0.01, ****P*<0.001, two-tailed Mann-Whitney *U* test. See also Figure S4.

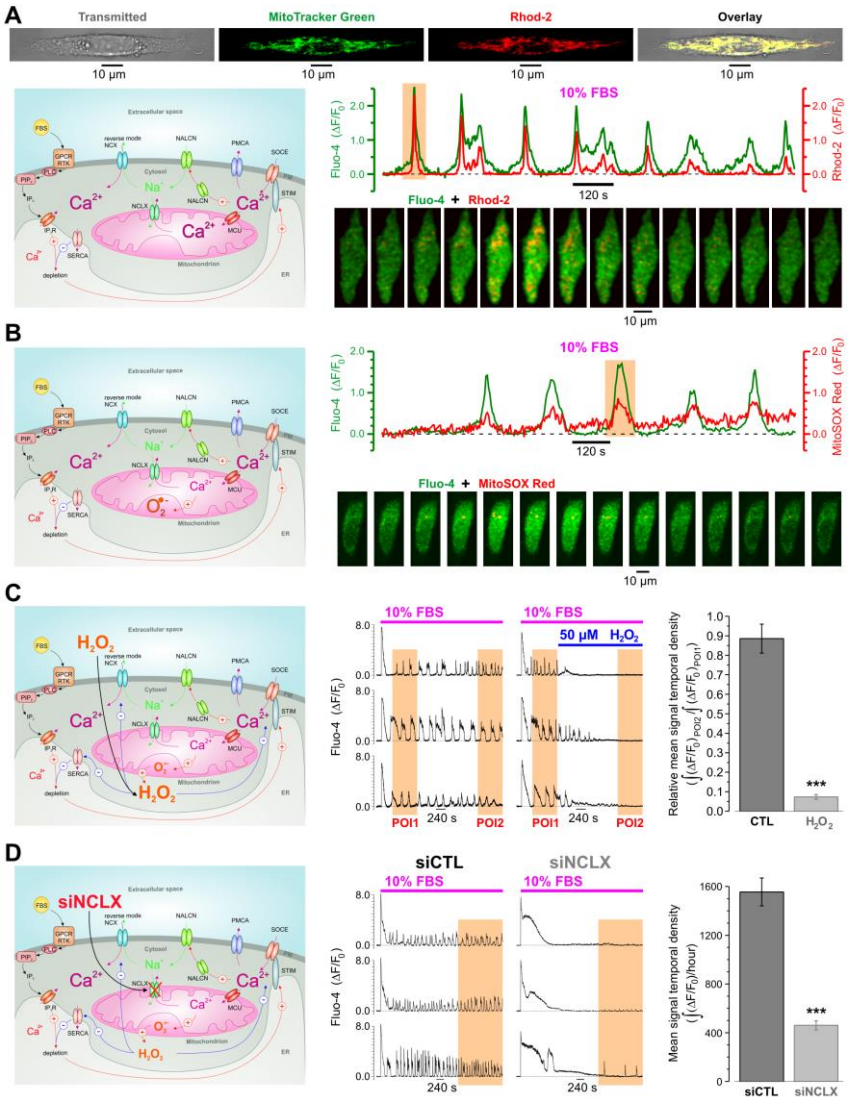

Figure 5. NALCN and Recruitment of Mitochondria to $[Ca^{2+}]_c$ Oscillations in PC-3 Cells.
Cartoons (left) highlight experimental design and assessed signaling pathways. Note that Na^+ delivered to the cytosol by NALCN, on the one hand, activates reverse mode (RM-) of NCX, while on the other hand, is exchanged by NCLX to Ca^{2+} thus restricting elevation of $[Ca^{2+}]$ in mitochondria ($[Ca^{2+}]_{mito}$) and, hence, production of superoxide (O_2^-) and H_2O_2, which is known to inhibit SERCA, RM-NCX and SOCE elements. (**a**) Top: visualisation of mitochondria with MitoTracker Green confirms mitochondrial origin of Rhod-2 signal. Middle: Fetal bovine serum (FBS)-induced $[Ca^{2+}]_c$ oscillations (Fluo-4) are associated with $[Ca^{2+}]_{mito}$ oscillations (Rhod-2). Bottom: every 2nd image from the highlighted (middle) period. (**b**) Top: FBS-induced $[Ca^{2+}]_c$ oscillations (Fluo-4) are associated with oscillations in O_2^- production by mitochondria (MitoSOX Red). Bottom: every 3rd image from the highlighted (middle) period. (**c**) O_2^- metabolite H_2O_2 suppresses FBS-induced $[Ca^{2+}]_c$ oscillations (Fluo-4). Left: representative traces. Right: mean signal (Fluo-4) temporal density during POI2 was normalized to that during POI1 in control (n=58) and in 50 µM of H_2O_2 (n=74), and compared. (**d**) Suppression of NCLX with siRNA (siNCLX) attenuates $[Ca^{2+}]_c$ oscillations (Fluo-4). Left: representative traces. Right: mean signal (Fluo-4) temporal densities during highlighted periods were compared in control (n=18) and following 48 h pre-treatment with siNCLX (n=17). Data are mean±S.E.M. ***P<0.001, two-tailed Mann-Whitney U test.

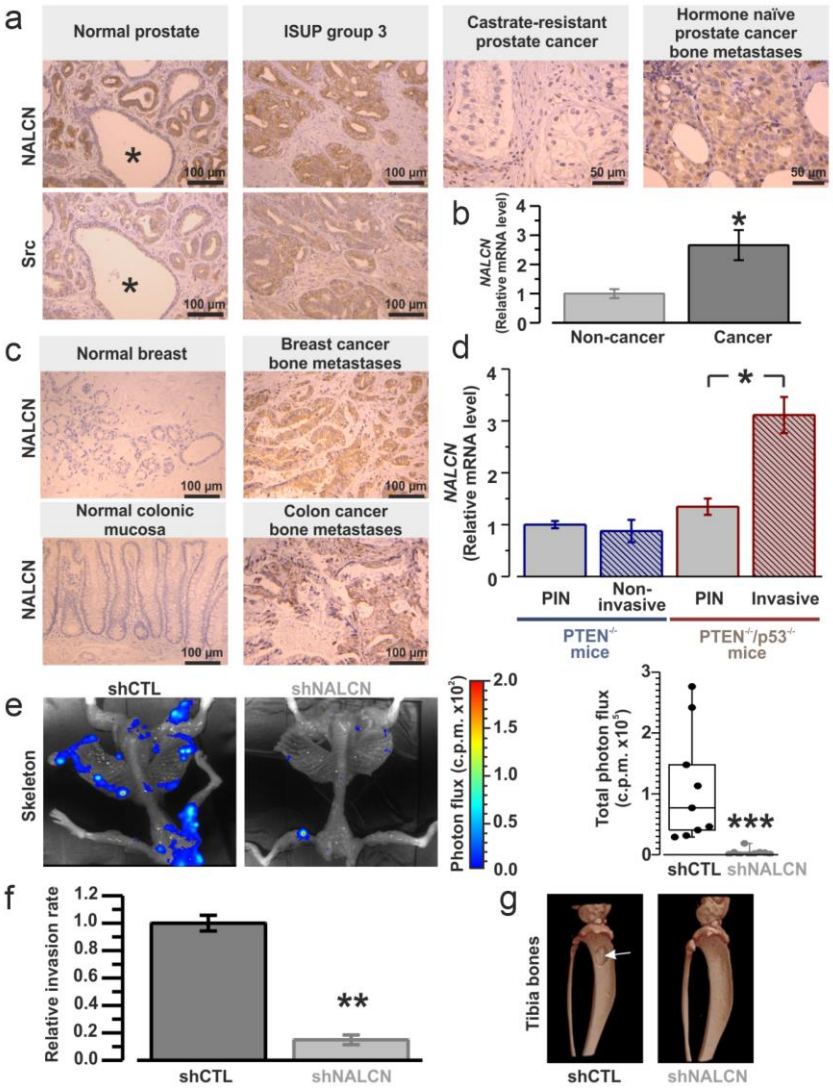

Figure 6. NALCN Promotes Prostate Cancer Progression.
(**a**) Immunohistochemistry: significant correlation (P<0.0001) between positive staining of NALCN and Src in clinically localized prostate cancer, but not in non-cancerous (*****) prostate. Note smooth muscle fibre staining as positive internal control for NALCN. (**b**) RT-qPCR: *NALCN* mRNA level in cancerous vs. non-cancerous prostate biopsies (n=28). Data are mean±S.E.M. *P<0.05, two-tailed Mann-Whitney U test. (**c**) Immunohistochemistry: positive staining of NALCN in bone metastases produced by breast and colon cancers, but not in normal corresponding tissues. (**d**) *NALCN* mRNA level was not different between prostatic intraepithelial neoplasia (PIN) and non-invasive prostate adenocarcinoma of PTEN$^{(i)pe-/-}$ mice. In contrast, invasive adenocarcinoma of PTEN/p53$^{(i)pe-/-}$ mice exhibited significant upregulation of NALCN mRNA when compared with corresponding PIN. Data from PTEN$^{(i)pe-/-}$ mice were normalized to control PTEN$^{(i)pe+/+}$ mice, whereas data from PTEN/p53$^{(i)pe-/-}$ mice - to control PTEN/p53$^{(i)pe+/+}$ mice. RT-qPCR data are normalized to *GAPDH* and *TBP* and presented as mean±SEM (n=5). *P<0.05, two-tailed Mann-Whitney U test. (**e**) *Ex vivo* bioluminescence images (BLIs) of skeleton metastases in mice 12 weeks after orthotopic injections of control (PC-3-Luc-shCTL) or NALCN depleted cells (PC-3-Luc-shNALCN). Right: box-plots with raw data of the BLI bone metastasis assay (n=10). Box-plots with raw data (n=10). ***P<0.001, two-tailed Mann-Whitney U test. (**f**) NALCN knockdown in PC-3 cells suppresses Transwell® (chemoattractant: conditioned media from osteoblasts) invasion from four independent experiments (n=4). Data are mean±S.E.M. **P<0.01, two-tailed Mann-Whitney U test. (**g**) X-ray 3D images: osteolysis (arrow) 31 days after intra-tibial injection of PC-3-Luc-shCTL or PC-3-Luc-shNALCN cells. See also Figures S5-S7 and Tables S1.

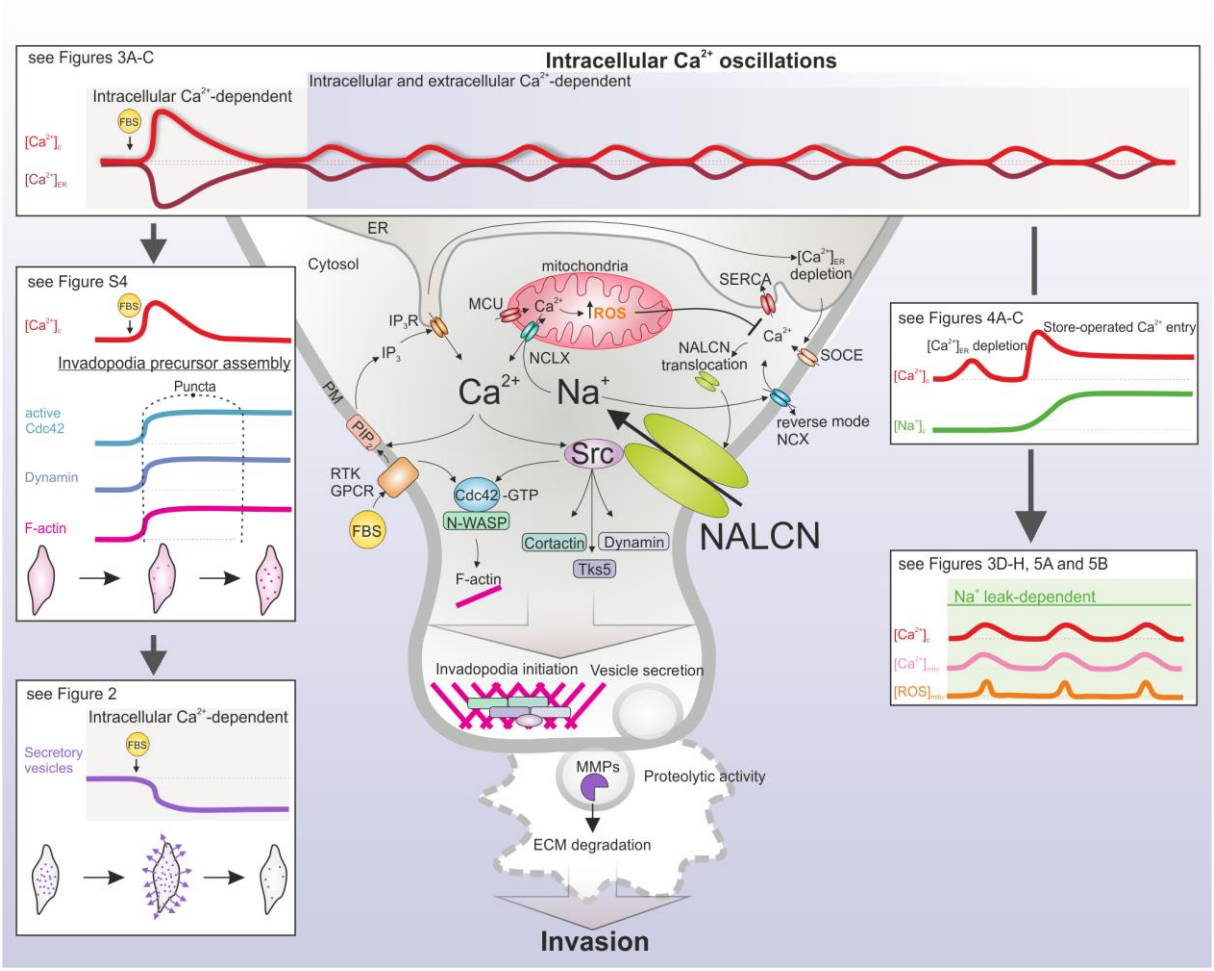

Figure 7. Schematic Representation of Signaling Pathways Employed by NALCN to Promote Cancer Cell Invasiveness.

Abbreviations: PM – plasma membrane, ER – endoplasmic reticulum, NALCN – Na^+ leak channel non-selective, RM-NCX – reverse mode of Na^+/Ca^{2+} exchanger, NCLX – mitochondrial Na^+/Ca^{2+} exchanger, IP_3R – inositol 1,4,5-trisphosphate receptor, SERCA –sarco/endoplasmic reticulum Ca^{2+}-ATPase, MCU – mitochondrial Ca^{2+} uniporter, RTK – receptor tyrosine kinases, GPCR – G-protein coupled receptors, Src – proto-oncogene Src tyrosine kinase, N-WASP – neural Wiskott-Aldrich syndrome protein, ECM – extracellular matrix, MMPs – matrix metalloproteinases, GTP – guanosine-5'-triphosphate, ROS – reactive oxygen species, $[Ca^{2+}]_c$ – cytosolic Ca^{2+} concentration, $[Ca^{2+}]_{ER}$ – Ca^{2+} concentration in ER, $[Ca^{2+}]_{mito}$ – Ca^{2+} concentration in mitochondria, $[Na^+]_c$ – cytosolic Na^+ concentration, $[ROS]_{mito}$ – ROS concentration in mitochondria.

Briefly: (i) IP_3R-mediated Ca^{2+} release caused by FBS-induced activation of RTK/GPCR causes the ER Ca^{2+} depletion and SOCE; elevation of $[Ca^{2+}]_c$ in sub-PM microdomains facilitates NALCN translocation to PM and Na^+ influx promoting RM-NCX and additional Ca^{2+} influx; this triggers SERCA-mediated Ca^{2+} uptake into the ER and MCU-mediated Ca^{2+} uptake into mitochondria; the latter facilitates production of ROS, known to inhibit SERCA (Qin et al., 2014), RM-NCX (Liu and O'Rourke, 2013) and SOCE elements (Bogeski et al., 2012), and is opposed by NCLX exchanging Na^+, delivered by NALCN, to mitochondrial Ca^{2+}; these positive and negative feedbacks give rise to $[Ca^{2+}]_c$ oscillations maintaining the activity Src, known as essential component of NALCN channelosome (Lu et al., 2009; Wang and Ren, 2009); active Src phosphorylates downstream proteins (cortactin, dynamin and Tks5) recruiting them to actin polymerization regions and giving rise to "invadopodia puncta". (ii) RTK/GPCR activation is linked to activation of the Rho family GTPase, Cdc42, leading to its binding with N-WASP and subsequent actin nucleation (Beaty and Condeelis, 2014). (iii) Invadopodia maturation is facilitated by Ca^{2+}-dependent secretion of MMPs degrading ECM.

See also Figures 2-3, 4A-C, 5A-B and S3.

BIBLIOGRAPHY

Barrett, T., Riemer, F., McLean, M.A., Kaggie, J., Robb, F., Tropp, J.S., Warren, A., Bratt, O., Shah, N., Gnanapragasam, V.J., et al. (2018). Quantification of Total and Intracellular Sodium Concentration in Primary Prostate Cancer and Adjacent Normal Prostate Tissue with Magnetic Resonance Imaging. Invest. Radiol. *53*, 450–456.

Bartha, R., Megyesi, J.F., and Watling, C.J. (2008). Low-grade glioma: Correlation of short echo time 1H-MR spectroscopy with 23Na MR imaging. Am. J. Neuroradiol. *29*, 464–470.

Beaty, B.T., and Condeelis, J. (2014). Digging a little deeper: The stages of invadopodium formation and maturation. Eur. J. Cell Biol. *93*, 438–444.

Ben-Kasus Nissim, T., Zhang, X., Elazar, A., Roy, S., Stolwijk, J.A., Zhou, Y., Motiani, R.K., Gueguinou, M., Hempel, N., Hershfinkel, M., et al. (2017). Mitochondria control store-operated Ca 2+ entry through Na + and redox signals. EMBO J. *36*, 797–815.

Berridge, M.J. (2008). Smooth muscle cell calcium activation mechanisms. J. Physiol.

Biankin, A. V., Waddell, N., Kassahn, K.S., Gingras, M.C., Muthuswamy, L.B., Johns, A.L., Miller, D.K., Wilson, P.J., Patch, A.M., Wu, J., et al. (2012). Pancreatic cancer genomes reveal aberrations in axon guidance pathway genes. Nature *491*, 399–405.

Bogeski, I., Kilch, T., and Niemeyer, B.A. (2012). ROS and SOCE: Recent advances and controversies in the regulation of STIM and Orai. J. Physiol. *590*, 4193–4200.

Brisson, L., Gillet, L., Calaghan, S., Besson, P., Le Guennec, J.Y., Roger, S., and Gore, J. (2011). Na v 1.5 enhances breast cancer cell invasiveness by increasing NHE1-dependent H efflux in caveolae. Oncogene *30*, 2070–2076.

Brisson, L., Driffort, V., Benoist, L., Poet, M., Counillon, L., Antelmi, E., Rubino, R., Besson, P., Labbal, F., Chevalier, S., et al. (2013). NaV1.5 Na+ channels allosterically regulate the NHE-1 exchanger and promote the activity of breast cancer cell invadopodia. J. Cell Sci. *126*, 4835–4842.

Catacuzzeno, L., and Franciolini, F. (2018). Role of KCa3.1 channels in modulating ca^{2+}oscillations during glioblastoma cell migration and invasion. Int. J. Mol. Sci.

Clapham, D.E. (2007). Calcium Signaling. Cell.

Cochet-Bissuel, M., Lory, P., and Monteil, A. (2014). The sodium leak channel, NALCN, in health and disease. Front. Cell. Neurosci. *8*.

Djamgoz, M.B.A., Fraser, S.P., and Brackenbury, W.J. (2019). In vivo evidence for voltage-gated sodium channel expression in carcinomas and potentiation of metastasis. Cancers (Basel). *11*, E1675.

Dolmetsch, R.E., Xu, K., and Lewis, R.S. (1998). Calcium oscillations increase the efficiency and specificity of gene expression. Nature *392*, 933–936.

Dupont, G., Combettes, L., Bird, G.S., and Putney, J.W. (2011). Calcium oscillations. Cold Spring Harb. Perspect. Biol. *3*, a004226.

Gillet, L., Roger, S., Besson, P., Lecaille, F., Gore, J., Bougnoux, P., Lalmanach, G., and Le Guennec, J.Y. (2009). Voltage-gated sodium channel activity promotes cysteine cathepsin-dependent invasiveness and colony growth of human cancer cells. J. Biol. Chem. *284*, 8680–8691.

Haneder, S., Giordano, F.A., Konstandin, S., Brehmer, S., Buesing, K.A., Schmiedek, P., Schad, L.R., Wenz, F., Schoenberg, S.O., and Ong, M.M. (2015). 23Na-MRI of recurrent glioblastoma multiforme after intraoperative radiotherapy: technical note. Neuroradiology *57*, 321–326.

Henzler, T., Konstandin, S., Schmid-Bindert, G., Apfaltrer, P., Haneder, S., Wenz, F., Schad, L., Manegold, C., Schoenberg, S.O., and Fink, C. (2012). Imaging of tumor viability in lung cancer: Initial results using23Na-MRI. RoFo Fortschritte Auf Dem Gebiet Der Rontgenstrahlen Und Der Bildgeb. Verfahren *184*, 340–344.

House, C.D., Vaske, C.J., Schwartz, A.M., Obias, V., Frank, B., Luu, T., Sarvazyan, N., Irby, R., Strausberg, R.L., Hales, T.G., et al. (2010). Voltage-gated Na+channel SCN5A is a key regulator of a gene transcriptional network that controls colon cancer invasion. Cancer Res. *70*, 6957–6967.

Huang, L., Zhang, Z., Qu, B., Cui, Z., Wang, Y., Li, J., Wang, J., Zuo, Z., Zhuo, Y., Yu, X., et al. (2018). Imaging of Sodium MRI for Therapy Evaluation of Brain Metastase with Cyberknife at 7T: A Case Report. Cureus *10*, e2502.

Iamshanova, O., Fiorio Pla, A., and Prevarskaya, N. (2017). Molecular mechanisms of tumour invasion: regulation by calcium signals. J. Physiol. *595*, 3063–3075.

Jacobs, M.A., Ouwerkerk, R., Wolff, A.C., Gabrielson, E., Warzecha, H., Jeter, S., Bluemke, D.A., Wahl, R., and Stearns, V. (2011). Monitoring of neoadjuvant chemotherapy using multiparametric,23Na sodium MR, and multimodality (PET/CT/MRI) imaging in locally advanced breast cancer. Breast Cancer Res. Treat. *128*, 119–126.
Jospin, M., Watanabe, S., Joshi, D., Young, S., Hamming, K., Thacker, C., Snutch, T.P., Jorgensen, E.M., and Schuske, K. (2007). UNC-80 and the NCA Ion Channels Contribute to Endocytosis Defects in Synaptojanin Mutants. Curr. Biol. *17*, 1595–1600.
Kwiatkowska, A., Didier, S., Fortin, S., Chuang, Y., White, T., Berens, M.E., Rushing, E., Eschbacher, J., Tran, N.L., Chan, A., et al. (2012). The small GTPase RhoG mediates glioblastoma cell invasion. Mol. Cancer *11*.
Laymon, C.M., Oborski, M.J., Lee, V.K., Davis, D.K., Wiener, E.C., Lieberman, F.S., Boada, F.E., and Mountz, J.M. (2012). Combined imaging biomarkers for therapy evaluation in glioblastoma multiforme: Correlating sodium MRI and F-18 FLT PET on a voxel-wise basis. Magn. Reson. Imaging *30*, 1268–1278.
Leslie, T.K., James, A.D., Zaccagna, F., Grist, J.T., Deen, S., Kennerley, A., Riemer, F., Kaggie, J.D., Gallagher, F.A., Gilbert, F.J., et al. (2019). Sodium homeostasis in the tumour microenvironment. Biochim. Biophys. Acta - Rev. Cancer *1872*, 188304.
Liu, T., and O'Rourke, B. (2013). Regulation of the Na+/Ca2+ exchanger by pyridine nucleotide redox potential in ventricular myocytes. J. Biol. Chem. *288*, 31984–31992.
Lu, T.Z., and Feng, Z.P. (2012). NALCN: A regulator of pacemaker activity. Mol. Neurobiol. *45*, 415–423.
Lu, B., Su, Y., Das, S., Liu, J., Xia, J., and Ren, D. (2007). The Neuronal Channel NALCN Contributes Resting Sodium Permeability and Is Required for Normal Respiratory Rhythm. Cell *129*, 371–383.
Lu, B., Su, Y., Das, S., Wang, H., Wang, Y., Liu, J., and Ren, D. (2009). Peptide neurotransmitters activate a cation channel complex of NALCN and UNC-80. Nature *457*, 741–744.
Lu, B., Zhang, Q., Wang, H., Wang, Y., Nakayama, M., and Ren, D. (2010). Extracellular Calcium Controls Background Current and Neuronal Excitability via an UNC79-UNC80-NALCN Cation Channel Complex. Neuron *68*, 488–499.
Monk, M., and Holding, C. (2001). Human embryonic genes re-expressed in cancer cells. Oncogene *20*, 8085–8091.
Monteith, G.R., Prevarskaya, N., and Roberts-Thomson, S.J. (2017). The calcium-cancer signalling nexus. Nat. Rev. Cancer *17*, 367–380.
Moshfegh, Y., Bravo-Cordero, J.J., Miskolci, V., Condeelis, J., and Hodgson, L. (2014). A Trio-Rac1-Pak1 signalling axis drives invadopodia disassembly. Nat. Cell Biol. *16*, 571–583.
Onganer, P.U., Seckl, M.J., and Djamgoz, M.B.A. (2005). Neuronal characteristics of small-cell lung cancer. Br. J. Cancer *93*, 1197–1201.
Ouwerkerk, R., Bleich, K.B., Gillen, J.S., Pomper, M.G., and Bottomley, P.A. (2003). Tissue Sodium Concentration in Human Brain Tumors as Measured with 23 Na MR Imaging. Radiology *227*, 529–537.
Ouwerkerk, R., Jacobs, M.A., MacUra, K.J., Wolff, A.C., Stearns, V., Mezban, S.D., Khouri, N.F., Bluemke, D.A., and Bottomley, P.A. (2007). Elevated tissue sodium concentration in malignant breast lesions detected with non-invasive 23Na MRI. Breast Cancer Res. Treat. *106*, 151–160.
Parisotto, M., Grelet, E., El Bizri, R., Dai, Y., Terzic, J., Eckert, D., Gargowitsch, L., Bornert, J.-M., and Metzger, D. (2018). PTEN deletion in luminal cells of mature prostate induces replication stress and senescence in vivo. J. Exp. Med. *215*, 1749–1763.
Pasti, L., Volterra, A., Pozzan, T., and Carmignoto, G. (1997). Intracellular calcium oscillations in astrocytes: A highly plastic, bidirectional form of communication between neurons and astrocytes in situ. J. Neurosci. *17*, 7817–7830.
Patel, F., and Brackenbury, W.J. (2015). Dual roles of voltage-gated sodium channels in development and cancer. Int. J. Dev. Biol. *59*, 357–366.
Prevarskaya, N., Skryma, R., and Shuba, Y. (2018). Ion Channels in Cancer: Are Cancer Hallmarks Oncochannelopathies? Physiol. Rev. *98*, 559–621.
Qin, F., Siwik, D.A., Pimentel, D.R., Morgan, R.J., Biolo, A., Tu, V.H., Kang, Y.J., Cohen, R.A., and Colucci, W.S. (2014). Cytosolic H2O2 mediates hypertrophy, apoptosis, and decreased SERCA activity in mice with chronic hemodynamic overload. Am. J. Physiol. Circ. Physiol. *306*, H1453–H1463.

Rizaner, N., Onkal, R., Fraser, S.P., Pristerá, A., Okuse, K., and Djamgoz, M.B.A. (2016). Intracellular calcium oscillations in strongly metastatic human breast and prostate cancer cells: control by voltage-gated sodium channel activity. Eur. Biophys. J. *45*, 735–748.
Roger, S., Gillet, L., Le Guennec, J.Y., and Besson, P. (2015). Voltage-gated sodium channels and cancer: Is excitability their primary role? Front. Pharmacol. *6*.
Santiago-Medina, M., Gregus, K.A., Nichol, R.H., O'Toole, S.M., and Gomez, T.M. (2015). Regulation of ECM degradation and axon guidance by growth cone invadosomes. Development *142*, 486–496.
Savineau, J.-P., and Marthan, R. (2000). Cytosolic Calcium Oscillations in Smooth Muscle Cells. News Physiol. Sci.
Shah, K., Patel, S., Mirza, S., and Rawal, R.M. (2018). Unravelling the link between embryogenesis and cancer metastasis. Gene *642*, 447–452.
Short, C.A., Suarez-Zayas, E.A., and Gomez, T.M. (2016). Cell adhesion and invasion mechanisms that guide developing axons. Curr. Opin. Neurobiol. *39*, 77–85.
Smedler, E., and Uhlén, P. (2014). Frequency decoding of calcium oscillations. Biochim. Biophys. Acta - Gen. Subj. *1840*, 964–969.
Sun, J., Lu, F., He, H., Shen, J., Messina, J., Mathew, R., Wang, D., Sarnaik, A.A., Chang, W.C., Kim, M., et al. (2014). STIM1- and Orai1-mediated Ca2+oscillation orchestrates invadopodium formation and melanoma invasion. J. Cell Biol. *207*, 535–548.
Takahashi, N., Chen, H.Y., Harris, I.S., Stover, D.G., Selfors, L.M., Bronson, R.T., Deraedt, T., Cichowski, K., Welm, A.L., Mori, Y., et al. (2018). Cancer Cells Co-opt the Neuronal Redox-Sensing Channel TRPA1 to Promote Oxidative-Stress Tolerance. Cancer Cell *33*, 985-1003.e7.
Tang, J., Guo, Y.-S., Yu, X.-L., Huang, W., Zheng, M., Zhou, Y.-H., Nan, G., Wang, J.-C., Yang, H.-J., Yu, J.-M., et al. (2015). CD147 reinforces $[Ca^{2+}]_i$ oscillations and promotes oncogenic progression in hepatocellular carcinoma. Oncotarget *6*, 34831–34845.
Topalidou, I., Chen, P.A., Cooper, K., Watanabe, S., Jorgensen, E.M., and Ailion, M. (2017). The NCA-1 and NCA-2 Ion channels function downstream of Gq and Rho to regulate locomotion in Caenorhabditis elegans. Genetics *206*, 265–282.
Verkhratsky, A., Trebak, M., Perocchi, F., Khananshvili, D., and Sekler, I. (2018). Crosslink between calcium and sodium signalling. Exp. Physiol. *103*, 157–169.
Wakai, T., Vanderheyden, V., and Fissore, R.A. (2011). Ca2+signaling during mammalian fertilization: Requirements, players, and adaptations. Cold Spring Harb. Perspect. Biol. *3*, 1–23.
Wang, H., and Ren, D. (2009). UNC80 functions as a scaffold for Src kinases in NALCN channel function. Channels *3*, 161–163.
Yeh, E., Ng, S., Zhang, M., Bouhours, M., Wang, Y., Wang, M., Hung, W., Aoyagi, K., Melnik-Martinez, K., Li, M., et al. (2008). A putative cation channel, NCA-1, and a novel protein, UNC-80, transmit neuronal activity in C. elegans. PLoS Biol. *6*, 0552–0567.
Zaric, O., Pinker, K., Zbyn, S., Strasser, B., Robinson, S., Minarikova, L., Gruber, S., Farr, A., Singer, C., Helbich, T.H., et al. (2016). Quantitative Sodium MR Imaging at 7 T: Initial Results and Comparison with Diffusion-weighted Imaging in Patients with Breast Tumors. Radiology *280*, 39–48.

ACKNOWLEDGMENTS

We thank F. Cabon (Cancer Research Centre of Toulouse, France) and S. Fraser (Imperial College London, United Kingdom) for C4-2 and PC-3M cell lines, accordingly. We thank E. Dewailly (Inserm U1003, University of Lille, France) for help with reagents and cellular biology methods. We thank C. Slomianny, E. Richard and A.-S. Lacoste of the BICeL- Campus Scientific City Facility for access to instruments and technical advices. We are indebted to the Research Federation FRABio (University of Lille, CNRS, FR 3688, FRABio, Biochimie Structurale et Fonctionnelle des Assemblages Biomoléculaires) for providing the scientific and technical environment conducive to achieving this work. We thank Dr. C. Lemmers (Vectorology facility, PVM, Biocampus Montpellier, CNRS UMS3426) for lenvirus production. We thank C. Lagadec and R.-A. Toillon for help with their flow-cytometry facility (Inserm U908, University of Lille, France). We thank Daniel Metzger (Inserm U1258, University of Strasbourg, France) and Emmanuelle Germain (Inserm U1003, University of Lille, France) for providing us with cDNA from *PTEN* null mice model.

O. I. was funded by the Ligue Nationale Contre le Cancer, France (GB/MA/CD 11813) and Laboratory of Excellence in Ion Channel Science and Therapeutics. H. I. is co-funded by both Naresuan University (Thailand) and the French Embassy in Thailand. The research in the authors' laboratory is supported by INSERM, la Ligue Nationale Contre le Cancer (équipe labellisée), Institute for Cancer Research (grant 2014-166); Le Ministere de l'Education Nationale, the Region Nord/Pas-de-Calais, la Fondation de Recherche Medicale, and l'Association pour la Recherche sur le Cancer.

AUTHOR CONTRIBUTIONS

O.I., D.G., Ar.M. and N.P. conceived and planned the study. O.I. and A.F. designed, performed and analyzed cell culture assays (e.g. cell cycle analysis, cellular viability, apoptosis, proliferation, cellular motility, wound-healing, Transwell® migration and invasion assays) as well as invadopodia fractionation and Src-family kinase activity assay. D.G. designed, performed and analyzed confocal microscopy experiments. O.I., A.F., R.D., E.D. and A.B. designed, performed and analyzed cellular and molecular biology experiments (e.g. RT-qPCR, immunoblotting, biotinylation, zymography). G.S., P.M. and A.F. designed, performed and analyzed electrophysiological recordings. O.I., A.F. and P.M. designed, performed and analyzed Ca^{2+} and Na^{+} imaging experiments. Ar.M. constructed NALCN-expressing plasmids. V.L. participated in choosing the epitope for antibody against NALCN. A.H. participated in the screening of shNALCN clones. L.A. and A.B. amplified and extracted plasmid constructs. H.I. and Ar.M. established PC-3 cell line stably overexpressing NALCN. C.S. designed, performed and analyzed time-lapse video microscopy, cellular motility and wound-healing experiments. L.B. and Se.R. designed, performed and analyzed measurements of intracellular pH. T.O. and S.M.-L. designed, performed and analyzed tumor growth and metastases in mice after orthotopical injections of PC-3 cells. Se.R., S.C.,

St.R., M.L., J.S. and S.L. designed, performed and analysed the bone metastatic model in mice after intracardiac injections of PC-3 cells. S.G. and P.C. designed, performed and analyzed osteoblasts-mediated invasion of PC-3 cells, intratibial injections of the latter and analysis of produced bone lesions. Ad.M. and P.G. performed immunohistochemical staining of prostate adenocarcinoma tissue microarray and V.L. helped them. G.F.-H. performed immunohistochemical staining of prostate biopsies from patients and analyzed the correlation between expression of different proteins. O.I., D.G., and N.P. wrote the manuscript and O.I., D.G., M.D., Se.R., Ar.M., P.C. and G.F.-H. reviewed it.